RSC Advances

PAPER

View Article Online
View Journal | View Issue

Cite this: *RSC Adv.*, 2026, **16**, 8772

High-performance anode material for Li-ion batteries from bismuth molybdate incorporating F-free binder

To Giang Tran, [ab] Thuy-An Nguyen,[cd] Viet Duc Phung, [cd] Dinh Quan Nguyen,[ef] Thanh Ngoc Nguyen,[gh] Dang Manh Le,[gh] Hieu Trung Bui,*[gh] Il Tae Kim, *[i] Tran Thi Kieu Ngan[i] and Tuan Loi Nguyen *[cd]

In the pursuit of high-performance anode materials for Li-ion batteries over the past few decades, bismuth molybdate (BMO) has emerged as a promising candidate. However, its interaction with traditional polyvinylidene fluoride (PVDF) binder is not favorable, leading to rapid degradation of cyclic capacity. Furthermore, PVDF is considered an environmentally toxic binder. Therefore, finding a suitable binder that enhances the cycle life of this material and is more environmentally friendly is essential. In this study, BMO material was successfully grown at a low annealing temperature (200 °C) in an air environment. Analyses including X-ray diffraction, transmission electron microscopy, and scanning electron microscopy coupled with energy-dispersive X-ray spectroscopy were employed to obtain a comprehensive understanding of the material morphology and structure. BMO was identified as a polycrystalline Bi_2MoO_6 material consisting of approximately 6.94 nm grains and 300–500 nm long rods with diameters ranging from 10 to 25 nm. In addition, an amorphous phase was observed in the BMO material. The effect of the binder on the electrochemical properties of BMO was evaluated using two binders: PVDF and poly(acrylic acid) (PAA). The BMO electrode using the PAA binder (BMO_PAA) demonstrated significantly better performance as an anode for lithium-ion batteries (LIBs) than that using the PVDF binder (BMO_PVDF). The BMO_PAA anode attained a 60th-cycle specific capacity of 738 mAh g^{-1} at 0.1 A g^{-1}, whereas this value for the BMO_PVDF electrode was 202 mAh g^{-1}. Therefore, this report presents the synthesis of a superior anode material for LIB fabrication that is compatible with a PAA binder, an environmentally friendly, fluorine-free binder.

Received 8th December 2025
Accepted 5th February 2026

DOI: 10.1039/d5ra09474g

rsc.li/rsc-advances

1. Introduction

With the global shift toward renewable energy sources and electric vehicles, lithium-ion batteries (LIBs) have become an exceptionally efficient and popular technology for storing energy. Owing to their high energy density, good stability, and wide commercialization, LIBs have been applied in mobile electronic devices, electric transport, and off-grid energy storage plants.[1–4] Nonetheless, the accelerated development of IoT devices and non-fossil fuels requires LIBs with higher capacity, faster charging speed, and longer cycle life. Therefore, new electrode materials are urgently needed. Among current commercial anodes, graphite is the most popular candidate because it exhibits high reversible-cycling durability while requiring little operating potential. However, graphite application expansion is constrained by its small theoretical capacity of only 372 mAh g^{-1}. In addition, the performance of graphite at high current rates is limited by slow lithium diffusion kinetics, which significantly reduces its fast-charging capability.[5–8] Therefore, the search for new-generation anode materials to replace graphite is a current focus of research. Conversion/alloying reactive materials have been investigated as alternative candidates because of their ability to store more electrons (their theoretical capacity is significantly larger than that of graphite).[9–12] However, these materials typically exhibit

[a]*Institute of Research and Development, Duy Tan University, Da Nang, Vietnam*
[b]*School of Engineering & Technology, Duy Tan University, Da Nang, Vietnam*
[c]*Institute of Fundamental and Applied Sciences, Duy Tan University, Ho Chi Minh City 70000, Vietnam. E-mail: nguyentuanloi@duytan.edu.vn*
[d]*Faculty of Environmental and Chemical Engineering, Duy Tan University, Da Nang City 50000, Vietnam*
[e]*Laboratory of Biofuel and Biomass Research, Faculty of Chemical Engineering, Ho Chi Minh City University of Technology (HCMUT), 268 Ly Thuong Kiet Street, Dien Hong Ward, Ho Chi Minh City, Vietnam*
[f]*Vietnam National University Ho Chi Minh City, Linh Xuan Ward, Ho Chi Minh City, Vietnam*
[g]*NTT Hi-Tech Institute, Nguyen Tat Thanh University, Ho Chi Minh City, Vietnam. E-mail: bthieu@ntt.edu.vn*
[h]*Nguyen Tat Thanh University Center for Hi-Tech Development, Saigon Hi-Tech Park, Ho Chi Minh City, Vietnam*
[i]*School of Chemical, Biological & Battery Engineering, Gachon University, Seongnam-si, Gyeonggi-do, 13120, Republic of Korea. E-mail: itkim@gachon.ac.kr*

common drawbacks, including poor conductivity and large volume changes, as an inevitable consequence of the lithiation–delithiation process, resulting in structural fracture and performance degradation after many cycles.[13,14] In this context, bismuth molybdate (Bi_2MoO_6) has emerged as a notable candidate owing to its superior properties. First, Bi_2MoO_6 belongs to the Aurivillius family and possesses the characteristic layered structure in which $(Bi_2O_2)^{2+}$ layers alternate with perovskite $(MoO_4)^{2-}$ blocks. These layers provide both structural stability and numerous lithium-ion insertion sites, thereby improving the capacity and ion diffusion rate. Second, the energy storage mechanism of Bi_2MoO_6 is contributed to by both the Bi^{3+}/Bi^0 and Mo^{6+}/Mo^0 redox pairs, allowing for higher theoretical capacities than those of many single-component metal oxides. Third, Bi can also form alloys with Li, contributing to increased capacity.[15,16]

In addition to the intrinsic properties of the active materials, the binder has a noticeable effect on the operational performance of LIB electrodes. The binder holds the active material particles together and fixes them on the current collector. It also contributes to maintaining mechanical strength during the charge–discharge cycle, which is often accompanied by significant volume expansion of the metal oxide materials.[17] The most common commercial anode binder is polyvinylidene fluoride (PVDF) because of its high chemical stability and ability to form durable films. However, PVDF requires toxic organic solvents such as *N*-methyl-2-pyrrolidone (NMP) and has limited flexibility, making the electrode susceptible to fracture under repeated mechanical stress.[18,19] Meanwhile, a new-generation binder based on poly(acrylic acid) (PAA) is more environmentally friendly and provides strong interaction with the material surface through hydrogen bonding or carboxyl groups, significantly improving cycling stability.[20] For materials with large volume changes, such as Bi_2MoO_6, the selection of an appropriate binder is considered crucial to minimize electrode structural degradation and improve long-term performance.

Currently, Bi and Mo-based materials are widely studied as anodes for high-performance LIBs.[21–30] However, these studies largely focus on fine-tuning the shape, structure, or aiming to enhance the specific surface area of the active material. To our knowledge, no studies have yet focused on investigating the suitability of binders with Bi_2MoO_6 materials to improve anode performance and create more environmentally friendly electrodes. Although several environmentally friendly binders also exhibit strong interactions with metal oxide materials, PAA and PVDF binders remain among the most widely used binders in previously reported studies on Bi- or Mo-oxide anode electrodes. The use of these two binders allows for a direct comparison of the effects of these two most common binders on Bi_2MoO_6 material and facilitates the interpretation of energy storage mechanisms. In this context, the PVDF binder is used as an electrochemically inert reference binder, while the PAA binder is used as a functional and environmentally friendly binder in studies focusing on interface chemistry and reaction kinetics.

In this study, we focused on the synthesis and evaluation of the electrochemical properties of anodes made of synthesized Bi_2MoO_6 (BMO). Our method for synthesizing BMO materials has been improved upon previous work.[21,31,32] Accordingly, we eliminated the high-temperature, long-duration hydrothermal treatment in autoclave step and switched the high-temperature annealing process from an Ar gas environment to air. These efforts aim for a simpler and more cost-effective synthesis method. The BMO material has a major Bi_2MoO_6 crystalline phase and a minor amorphous phase. With simple synthesis conditions at a low (roughly 200 °C) annealing temperature in an air environment, BMO is formed with a special morphology that includes particles of approximately 6.94 nm in diameter and rods of approximately 300–500 nm in length and 10–25 nm in diameter. The lithium-ion storage process and charge–discharge performance of the BMO electrode material were investigated using two different types of binders, PAA and PVDF. The BMO_PAA electrode displayed significantly better capacity retention, achieving 738 mAh g^{-1} at 0.1 A g^{-1} after 60 cycles, 3.65 times that of the BMO_PVDF electrode. In addition, the BMO_PAA electrode exhibited outstanding fast charging capability, reaching 566 mAh g^{-1} at 3 A g^{-1}. These properties suggest that BMO combined with the PAA binder has a strong potential to act as an anode for the next generation of the most widely used battery type.

2. Experimental

2.1. Synthesis of BMO

$Bi(NO_3)_3 \cdot 5H_2O$ and $Na_2MoO_4 \cdot 2H_2O$ salts were weighed separately at a Bi/Mo molar ratio of 1 : 1. The two salts were each dissolved in 40 mL of ethylene glycol (EG) solvent. The Na_2MoO_4 solution was heated to 80 °C under magnetic stirring. The $Bi(NO_3)_3$ solution was added dropwise, and the reaction was stirred at 80 °C for 2 h after the addition was complete. The resulting precipitate was centrifuged at 5000 rpm for 8 min and washed three times with distilled water and ethanol. Next, the solid was dried at 90 °C for 24 h before being annealed at 200 °C for 12 h in air (as illustrated in Fig. 1). The calcined product was designated as BMO, and its morphological and structural properties and its performance as a LIB electrode material were investigated.

2.2. Material properties

The morphological and structural properties of the BMO were examined using advanced methods. In particular, X-ray diffraction (XRD) was used to examine the phase composition of the BMO material with 2θ ranging from 10 to 80°. The ratio of the amorphous to crystalline phases in the BMO material was estimated based on the XRD results. The morphology of the BMO was investigated using three techniques: scanning electron microscopy (SEM), transmission electron microscopy (TEM), and high-resolution TEM (HRTEM). The elemental composition of BMO was studied using energy-dispersive X-ray spectroscopy (EDS). Raman spectroscopy was employed to confirm the composition and structural characteristics of the BMO material. Fourier Transform Infrared Spectroscopy (FTIR) analysis was used to identify the characteristic groups of the two binders.

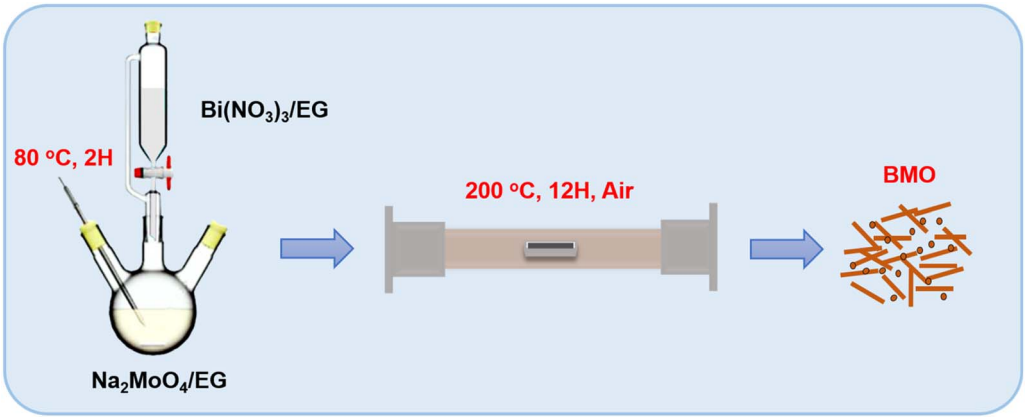

Fig. 1 Schematic diagram of Bi_2MoO_6 (BMO) material fabrication.

2.3. Electrochemical measurements

BMO anodes were built by blending the main components, including the BMO material, Super P, binder, and solvent. In this study, two different binders were used to investigate the compatibility of BMO with the binders in terms of the electrochemical performance of the electrode. Briefly, the PAA binder was combined with ethanol as a solvent, and the PVDF binder was processed using NMP as a solvent. After 12 h of stirring, the resulting homogeneous slurry was coated onto copper sheets using a doctor blade. The coated copper sheets were dried at 105 °C for 2 h to remove the solvent. Next, circular disks with a diameter of 1.5 cm were prepared from the dried sheets. The slurry-coated sheets used as working electrodes were then packed into coin cells together with Li foil (counter and reference electrodes) and Celgard 2400 (separator). The electrolyte was $LiPF_6$ (1 M) in a 1 : 1 mixture of diethyl carbonate and ethylene carbonate. The coin cell assembly was performed in a glove box (MBRAUN). Cyclic voltammetry (CV) measurements of the BMO electrodes were then performed using an Arbin instrument in the range 0.01–3 V at various scan rates from 0.3 to 1.2 mV s^{-1}. Constant-current charging and discharging processes were performed using a Neware instrument for cycling and rate tests. The electrochemical impedance spectroscopy (EIS) profiles of the BMO electrodes after the rate test were examined using a Gamry instrument over the range 1000 kHz–0.1 Hz. For comparison, two electrodes using graphite as the active material were also fabricated using a similar process with two types of binders, PVDF and PAA. All electrochemical measurements in this study were performed using at least three independently assembled cells under identical conditions. The data shown in the manuscript are representative results that closely match the average behavior observed from these repeated experiments.

3. Results and discussion

An XRD analysis was conducted on the BMO sample, and the results are shown in Fig. 2. The diffraction peaks appeared in the XRD pattern of BMO at 10.9, 23.5, 28.3, 32.6, 33.1, 36, 46.7, 47.1, 55.5, 56.2, 58.4, 75.4, and 75.9°. These peaks may be related to the (020), (111), (131), (002), (060), (151), (202), (260), (331), (191), (262), (333), and (391) planes of the Bi_2MoO_6 phase, respectively. No secondary phases (BiO, Bi_2O_3, or MoO_3) were detected in the synthesized material. This result demonstrates that the synthesis parameters, such as reaction time, temperature, and calcination duration, were controlled effectively to form the Bi_2MoO_6 phase. A slight increase in the baseline diffraction pattern suggests the presence of an amorphous phase coexisting with the crystalline phase in the synthesized material. The ratio between the amorphous and crystalline Bi_2MoO_6 phases in the material was determined using eqn (S1) and (S2). The results indicate that the BMO material contains both Bi_2MoO_6 crystalline and amorphous phases, of which the dominant crystalline phase accounts for approximately 87.8%. The Raman spectrum of the BMO material (Fig. S1) fully exhibits the characteristic vibrational modes in the Aurivillius structure of the Bi_2MoO_6 crystalline phase. Peaks at 88.9, 139.4, and 195.2 cm^{-1} are assigned to lattice modes related to the motion of Bi and Mo ions in the crystal lattice. Peaks at approximately 290.8, 320, 350.8, and 401.2 cm^{-1} belong to bending modes of the Mo–O bond in the MoO_6 octahedra. In the high-frequency region, peaks at 717.6, 796.1, and 846.7 cm^{-1} correspond to asymmetric stretching, symmetric stretching (A_{1g}), and orthorhombic distortion vibrations in

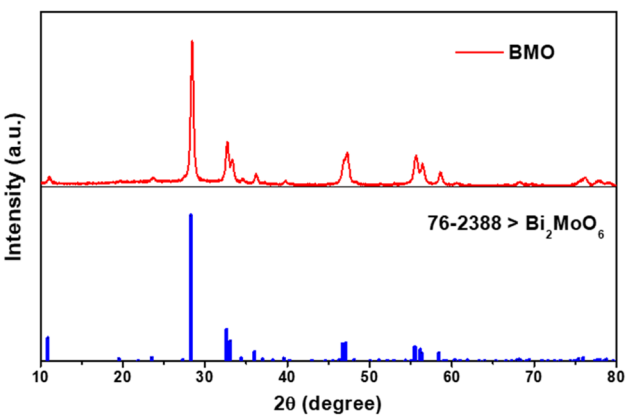

Fig. 2 X-ray diffraction (XRD) spectrum of the BMO sample.

MoO_6, respectively. These results are in good agreement with previous reports, confirming the successful formation of the Bi_2MoO_6 phase.[33,34]

The SEM images of the BMO material are shown in Fig. 3(a and b). The material consisted of rod-like structures and particles. The rods had lengths of roughly 300–500 nm and diameters of approximately 10–25 nm. The BMO material morphology and size was more clearly revealed in the TEM image in Fig. 3(c and d), where the particles were found to have an average size of approximately 6.94 nm, with approximately 89% distributed between 5 and 9 nm (Fig. 3e). They tended to aggregate into larger clusters and attach to the rod surfaces. The HRTEM image of the BMO material recorded d-values of about 2.75 Å and 3.26 Å, corresponding to the (002) and (041) crystal planes of the Bi_2MoO_6 phase. In addition, an amorphous region was observed in the material. Thus, the synthesized BMO was identified as polycrystalline Bi_2MoO_6 containing an amorphous component. Fig. 4 shows a mapping image of the elements in the BMO material at the micrometer level. Bi, Mo, and O were detected in the composite with a widespread, uniform distribution. The ratio of these elements (presented in Table S1) shows that the ratio of Bi, Mo, and O was 1.5 : 1 : 4.5, which slightly deviated from the theoretical ratio of the Bi_2MoO_6 phase. This deviation was attributed to the influence of the amorphous component in the BMO sample. These results were consistent with the XRD patterns.

The BMO material was fabricated into electrodes using two different binders, PVDF and PAA, referred to as BMO_PVDF and BMO_PAA electrodes, respectively. The FTIR results for the two binders, PVDF and PAA, are presented in Fig. S2. The

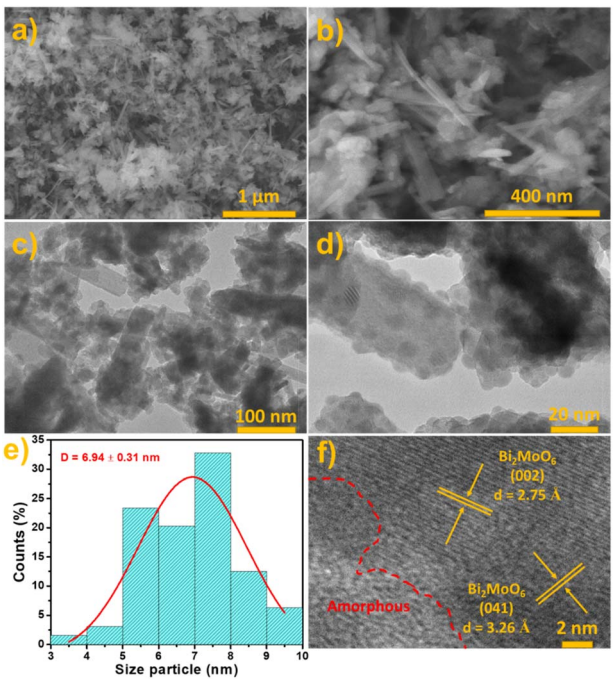

Fig. 3 (a and b) Scanning electron microscopy (SEM); (c and d) transmission electron microscopy (TEM); (e) histogram of particle size distribution; (f) high-resolution TEM (HRTEM) images of the BMO material.

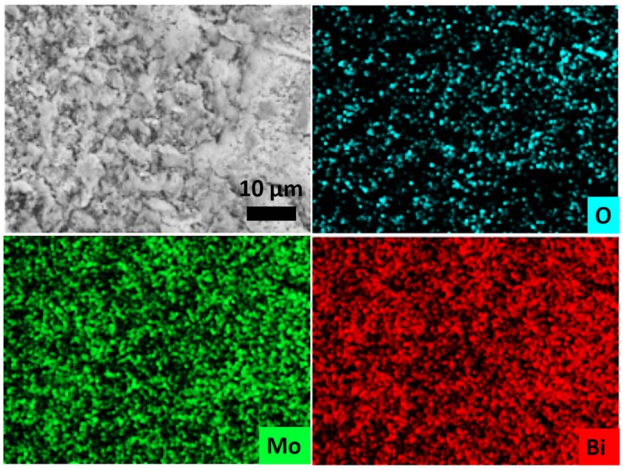

Fig. 4 Mapping image of elements of the BMO material.

characteristic peaks for both PVDF and PAA materials were observed on the FTIR curves of the two samples. Peaks related to C–F vibrations in the CF_2 group could be observed at 1184, 795, 764, and 614 cm^{-1}.[35–38] The characteristic COOH group of the PAA binder could be observed at 3500–2500, 1690, 1417, and 1210 cm^{-1}.[39–41] The CV curves of these electrodes were investigated and are presented in Fig. 5(a and b). The positions of the redox peaks observed in the CV curves of the two BMO electrodes were relatively similar. The cathodic peaks at 1.64 V and 0.55 V in the first cycle could be related to the insertion of Li^+ ions into the Bi_2MoO_6 structure (eqn (1)), reduction of Bi_2MoO_6 to form Bi and Mo (eqn (2)), alloying of Bi (eqn (3)), and the development of the SEI layer, respectively. In the next two cycles, these peaks separated and shifted to different positions because of the influence of SEI layer formation after the first cycle. The peaks at 2.01 V and 1.43 V were related to the reaction between Li^+ ions and Bi_2MoO_6, while the remaining peaks could be attributed to the alloying process forming the Li_3Bi phase. The oxidation peaks appeared at the same positions across the three cycles, corresponding to the de-alloying of Li_3Bi to Bi at 0.97 V and the oxidation of Bi and Mo to form Bi_2MoO_6 at the remaining peaks.[9,26,42] In addition, the CV curves of the BMO_PVDF electrode exhibited noticeable noise, suggesting a less stable oxidation process compared to that of the BMO_-PAA electrode.

$$Bi_2MoO_6 + aLi^+ + ae^- \leftrightarrow Li_aBi_2MoO_6 \quad (1)$$

$$Li_aBi_2MoO_6 + (12 - a)Li^+ + (12 - a)e^- \leftrightarrow 2Bi + Mo + 6Li_2O \quad (2)$$

$$Bi + 3Li^+ + 3e^- \leftrightarrow Li_3Bi \quad (3)$$

Fig. 5(c and d) presents the voltage profiles of the two BMO electrodes. The charge and discharge capacities of the BMO_-PAA electrode in the first cycle were higher than those of the BMO_PVDF electrode at 858/1131 and 659/987 mAh g^{-1}, respectively. In addition, the coulombic efficiency of the BMO_PVDF electrode was much lower than that of the

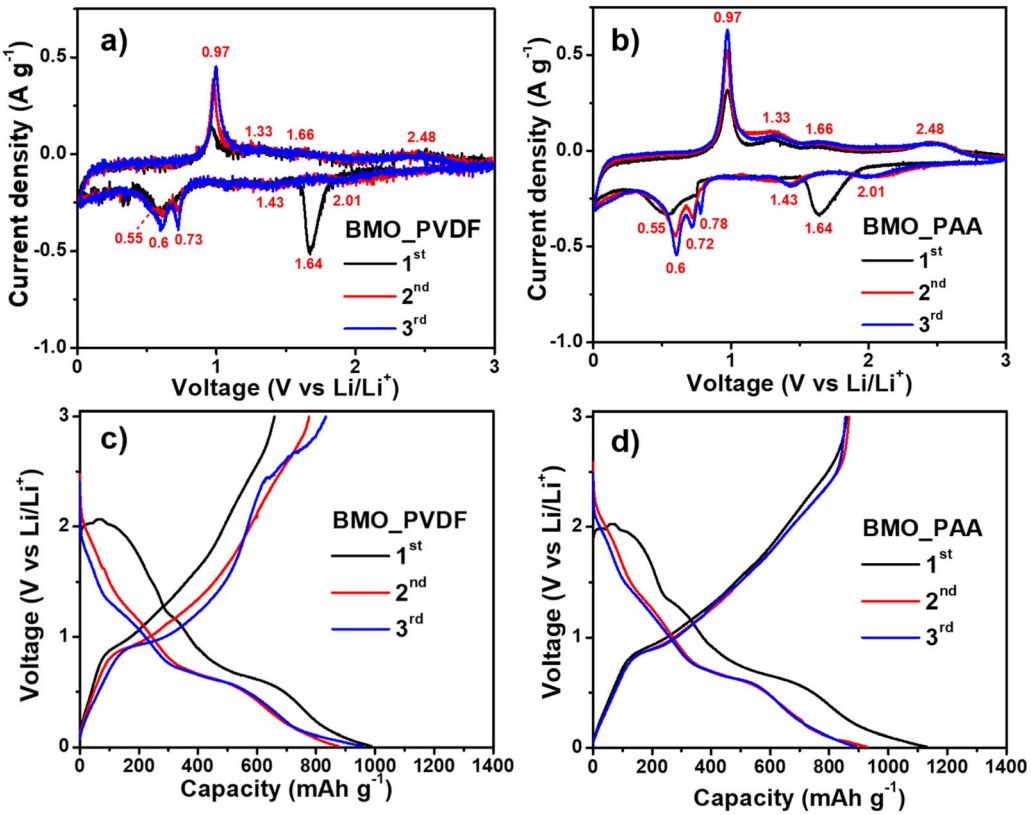

Fig. 5 (a and b) CV curves, (c and d) voltage profile plots of the BMO_PVDF and BMO_PAA electrodes.

BMO_PAA electrode. From the first to third cycles, efficiencies of 66.8%, 88.6%, and 86.9% were achieved for the BMO_PVDF electrode, which were significantly lower than the corresponding efficiencies of 75.9%, 93.4%, and 95.9% for the BMO_PAA electrode. These results indicate the poor reversibility of the BMO_PVDF electrode compared to the other electrodes. Furthermore, the voltage profiles of the two electrodes also show consistency with the CV curves. Specifically, in the first discharge cycle, broad plateaus extending in the 1.52–1.95 V and 0.2–0.79 V ranges are observed in the voltage profiles of the BMO electrodes. These may be related to the broad peaks at 1.64 V and 0.55 V in the CV curve, suggesting the reduction of Bi_2MoO_6 phase and the formation of the Li_3Bi alloy, respectively. During charging, a plateau from 0.82–1.15 V suggests the recovery of the Bi phase, which could be equivalent to a high-intensity peak of 0.97 V in the CV curve. The remaining steep slope may be the recording of the recovery of the Bi_2MoO_6 phase.[22,42,43]

The energy storage capacity of the BMO electrodes was investigated over 60 cycles at a current density of 0.1 A g^{-1}, as presented in Fig. 6a. During the initial few cycles, both electrodes exhibited relatively stable lithiation capacities with negligible variations. However, starting from the fifth cycle, a gradual capacity drain was observed in the PVDF electrode. By the 60th cycle, this electrode had almost lost its outstanding electrochemical performance in the initial cycles. The recorded specific capacity was approximately 202 mAh g^{-1}, indicating the typical failure behavior of metal-based anode materials when applied in LIBs. The BMO_PAA electrode, in contrast, exhibited stable capacities over successive cycles, forming a nearly horizontal straight line from the fifth cycle onward, with a value of about 738 mAh g^{-1} at the 60th cycle. It can be seen that the electrochemical performance of the BMO_PAA electrode is outstanding among previously reported bismuth anodes (Table S2). This phenomenon clearly indicated the capacity stability of the BMO_PAA electrode during cycling. The specific capacity over cycles of two graphite electrodes using two PAA and PVDF binders was investigated and the results are presented in Fig. S3. Unlike the electrodes using BMO material, the graphite electrodes showed good capacity retention over cycles in both electrodes using the two different binders. Specifically, after 50 cycles, the capacity remained at 416 mAh g^{-1} with the Graphite_PAA electrode and 476 mAh g^{-1} with the PVDF electrode. This not only demonstrates the electrochemical performance of traditional graphite material less affected by the binder but also shows a strong difference in the cycle strength of the graphite-based anode electrode compared to the metal-based BMO electrode when changing binders.

Next, the high current density performance of the BMO electrodes prepared with the two different binder types was evaluated, as shown in Fig. 6b. During the first five cycles, the charge capacities of the two electrodes were similar. As the current intensity increased, the difference became more apparent. The BMO_PAA electrode exhibited a low capacity loss of only 13% at a current density of 3 A g^{-1}, whereas the BMO_PVDF electrode showed a substantial capacity loss of 37%

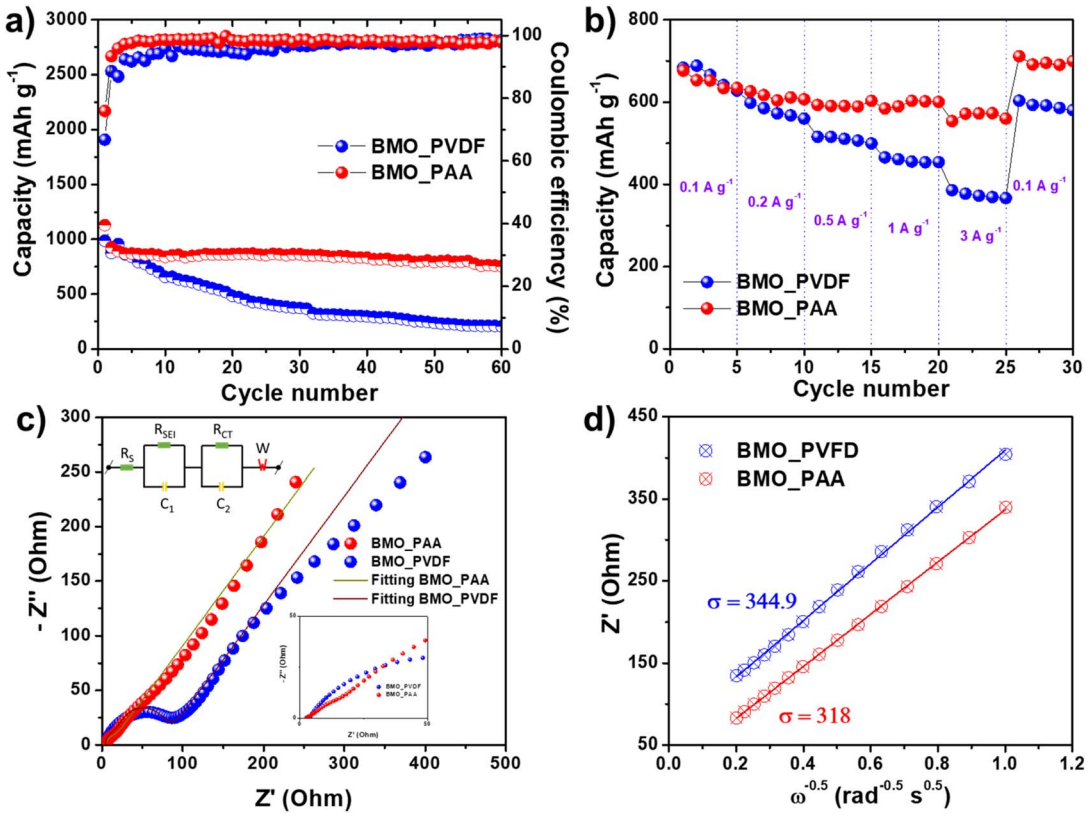

Fig. 6 (a) Cycling performance, (b) rate performance, (c) Nyquist curves, and (d) the correlation of Z' *vs.* $\omega^{-0.5}$ of BMO_PVDF and BMO_PAA electrodes.

at the same current density. When the current density returned to 0.1 A g^{-1}, the capacities of the electrodes increased to 588 and 697 mAh g^{-1}, corresponding to the BMO_PVDF and BMO_PAA electrodes. These results revealed that the electrode prepared using the BMO material in combination with the PVDF binder exhibited poorer fast-charging performance than the electrode prepared using the PAA binder. To explain this phenomenon, EIS measurements were performed on both electrodes after the rate tests. Fig. 6c displays the Nyquist curves and the equivalent circuits of the two BMO electrodes. The semicircles in the Nyquist curves appearing in the high-to mid-frequency range can be attributed to the SEI layer resistance (R_{SEI}) and charge transfer resistance (R_{ct}). The remaining straight lines can be attributed to the diffusion of Li^+ ions into the electrode material. Table S3 lists the details of the resistance parameters of the electrodes obtained using the fitting method. Obviously, the solvent resistances of the two electrodes showed a minor difference, measured at 3.92 Ω for the BMO_PVDF electrode and 2.55 Ω for the BMO_PAA electrode. However, the SEI and charge-transfer resistances of the two electrodes were significantly different, with the BMO_PVDF electrode exhibiting a value more than 10 times that of the BMO_PAA electrode. This large difference may be due to surface fractures and stress after rate testing of BMO_PVDF electrode. Fig. 6d displays the relationship between Z' and $\omega^{-0.5}$ of the two electrodes. The BMO_PAA electrode had a smaller Warburg coefficient (σ) than the BMO_PVDF electrode, indicating that the diffusion of Li^+ ions in the BMO_PAA electrode is more favorable. This explains the better fast-charging ability of the BMO_PAA electrode compared to that of the BMO_PVDF electrode. The superior electrochemical performance of the BMO_PAA electrode can be attributed to the enhanced bonding between the electrode material and the carbon black provided by the PAA binder, which improved the cycling durability of the electrode. This property is attributed to the –COOH functional groups in the PAA binder, which form strong coordination interactions with the metal-based active material and promote strong adhesion among the components, including the active material, carbon black, and current collector.[44–46] This interaction contributes to the formation of a continuous and stable electrode material network, enabling this electrode to accommodate better the volume expansion and contraction associated with repeated lithiation/delithiation processes during cycling. By contrast, the PVDF binder, which is a weakly polar polymer, cannot effectively withstand the stress of structural expansion. Therefore, significant volume changes in the metal anode material can readily cause surface fracture, resulting in increased resistance and degradation of the electrochemical performance.[47,48] XRD (Fig. S4) and SEM (Fig. S5) analyses of the BMO electrodes before and after the cycling test were performed to better understand the charge–discharge mechanism and surface morphology of the electrodes during battery operation. The XRD results of both electrodes before the cycling test showed similar spectral shapes. However, after 60 cycles, the diffraction

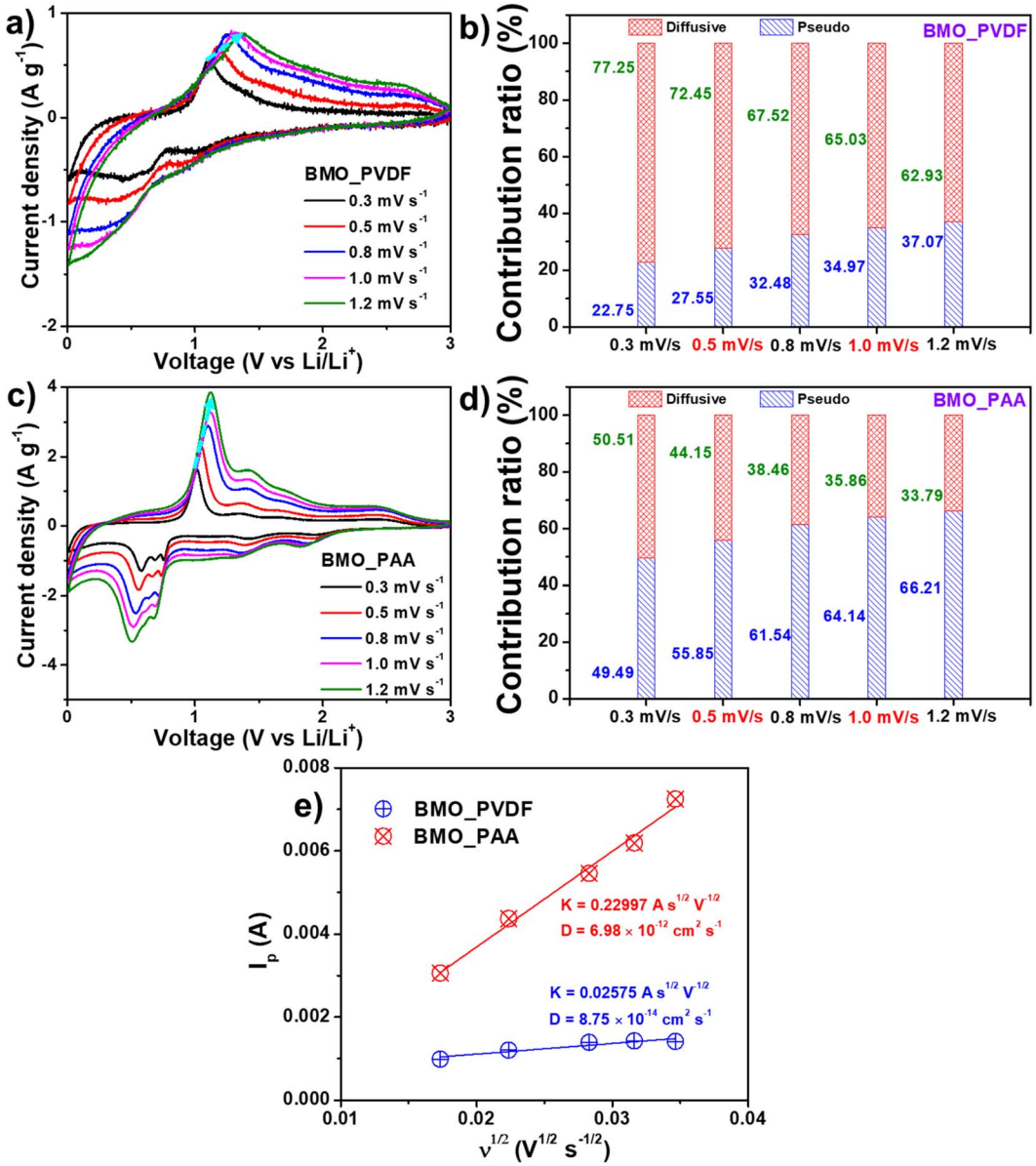

Fig. 7 (a and c) CV curves and (b and d) the ratio of the capacitive contribution for the BMO_PVDF and BMO_PAA electrodes at scan rates. (e) Relationships between I_p and $\nu^{1/2}$ of the BMO electrodes.

peaks on the two electrodes showed slight differences. Peaks related to the Bi_2MoO_6 and Bi_2O_3 phases were recorded on both electrodes after cycling. Notably, the BMO_PVDF electrode after cycling showed several peaks possibly related to the Li_2O, Li_2CO_3, and MoO_3 phases. These peaks were clearly observed on the BMO_PVDF electrode but were absent on the BMO_PAA electrode. These findings suggest the formation of a dense SEI layer on the BMO_PVDF electrode compared to the BMO_PAA electrode. SEM images of the BMO electrodes after cycling further support this argument. The surface morphology of the two BMO electrodes before cycling was observed to be almost identical. After cycling, the BMO_PVDF electrode showed a dense film, possibly an SEI layer, which did not occur with the BMO_PAA electrode. This result partly explains the significantly higher SEI resistance value of the BMO_PVDF electrode compared to the other electrode. Furthermore, direct electrode surface imaging also showed that the coating material peeled off the copper foil for the BMO_PVDF electrode, while it remained well-adhered and almost intact for the BMO_PAA electrode. These results demonstrate the suitability of PAA binder over PVDF when combined with BMO material as an anode material for LIBs.

Fig. 7(a and c) exhibits the CV curves of the two BMO electrodes at different scanning rates. Redox peaks representing the Bi_2MoO_6 phases were clearly observed in the CV curves of the PAA electrode. In contrast, although these peaks appeared in the initial cycles of the BMO_PVDF electrode (Fig. 5a), they became significantly weaker in subsequent cycles. This phenomenon indicated that the electrochemical activity of the BMO anode material gradually diminished when PVDF was

used as the binder. The BMO material with the PAA binder performed well, even at high potential scanning rates. The CV curves were further decomposed into two components, the pseudo- and diffusion components (Fig. S6 and S7), by solving the mathematical matrix.[49] The contribution ratio between the two components obtained for the BMO electrodes is shown in Fig. 7(b and d). The pseudo-component of the BMO_PAA electrode was consistently higher, ranging from 1.79 to 2.18 times that of the BMO_PVDF electrode at all scan rates. The reason for the increased pseudo-component of the BMO_PAA electrode compared to the BMO_PVDF electrode may be due to the –COOH groups of PAA binder. These may form hydrogen bonds or ionic interactions with the metal oxide surfaces, resulting in stronger adhesion and changes in the bonding structure between the active material and the binder. This leads to the creation of a better dispersed electrode surface, increasing the electrochemical contact surface area with the electrolyte, facilitating fast faradaic reactions at the surface, resulting in increased pseudocapacitance.[50–52] Meanwhile, PVDF is just an inert polymer, not involved in this interaction, so the electrode has less active surface area. The dominance of the pseudo-behavior of the BMO_PAA electrode suggests that this electrode can store energy quickly through redox reactions on its surface. The Li^+ ion diffusion coefficient of the two BMO electrodes was calculated using CV curves (Fig. 7e) by the Randles–Sevcik equation, which has been detailed in previous reports.[53,54] The results show that the Li^+ ion diffusion coefficient of the BMO_PAA electrode was nearly 80 times higher than that of the BMO_PVDF electrode. This is consistent with the experimental results obtained from the rate and EIS tests.

4. Conclusions

In summary, this study presents a method for the fabrication of polycrystalline Bi_2MoO_6 material containing an amorphous phase using $Bi(NO_3)_3$ and Na_2MoO_4 as precursors, in which the annealing process is controlled at a low temperature in an air environment to reduce the fabrication cost. Advanced characterization methods were performed, showing that the synthesized material reached the nanometer scale with approximately 6.94 nm particles that agglomerated into large clusters and aggregated around rod-like structures 300–500 nm in length and 10–25 nm in diameter. When employed as an anode material for LIBs with PAA as the binder, the BMO electrode exhibited a high specific capacity of approximately 858/1131 mAh g^{-1} in the first cycle. Moreover, after 60 continuous charge–discharge cycles, this electrode retained more than 86% of its charge capacity. The BMO_PAA electrode demonstrated an outstanding rate performance with a charge capacity of 566 mAh g^{-1} at 3 A g^{-1}. In addition, the electrochemical superiority, particularly the long cycling stability, of the electrode using the PAA binder compared to that using the PVDF binder was investigated and clarified. The high electrochemical performance of the BMO_PAA electrode may be affected by several factors: (i) the Bi_2MoO_6 phase exhibits both conversion and alloying mechanisms when storing Li ions, thereby enhancing the specific capacity of BMO material;[21,43] (ii) the nanoscale morphology of the BMO material shortens the Li ion diffusion path and increases the contact ability of the active material with the electrolyte;[55–57] (iii) the amorphous phase contributes to increased cycling stability by acting as a buffer layer to reduce structural stress during battery expansion;[58,59] and (iv) the use of an appropriate PAA binder enhances the interaction and tight bonding among the anode electrode components, thereby improving the cycling stability of the anode electrode.

Author contributions

To Giang Tran: formal analysis, investigation; Thuy-An Nguyen: methodology; Viet Duc Phung: formal analysis; Dinh Quan Nguyen: resources; Thanh Ngoc Nguyen: data curation; Dang Manh Le: investigation; Hieu Trung Bui: writing – original draft; Il Tae Kim: writing – original draft; Tran Thi Kieu Ngan: visualization; Tuan Loi Nguyen: conceptualization, funding acquisition, supervision, writing – review, and editing.

Conflicts of interest

There are no conflicts to declare.

Data availability

Additional supporting data are provided in the supplementary information (SI) accompanying this article. Supplementary information is available. See DOI: https://doi.org/10.1039/d5ra09474g.

Acknowledgements

This research was funded by Vietnam National Foundation for Science and Technology Development (NAFOSTED) under grant number 104.06-2025.66. We acknowledge Nguyen Tat Thanh University, Ho Chi Minh City, Vietnam, for supporting this study. This work was supported by the Gachon University research fund of 2025(202503110001).

References

1 S. Babu Sanker and R. Baby, *J. Energy Storage*, 2022, **50**, 104606.
2 X. Zhang, Z. Li, L. Luo, Y. Fan and Z. Du, *Energy*, 2022, **238**, 121652.
3 K. Yang, Y. Huang, P. Wang, Y. Tang, Y. Zhu, X. Zhu, Y. Xu, W. Jiang, L. Pan, Q. Li, H. Xie and J. Yang, *Chem. Eng. J.*, 2024, **486**, 150416.
4 B. Scrosati and J. Garche, *J. Power Sources*, 2010, **195**, 2419–2430.
5 H. Zhang, Y. Yang, D. Ren, L. Wang and X. He, *Energy Storage Mater.*, 2021, **36**, 147–170.
6 S. Weng, G. Yang, S. Zhang, X. Liu, X. Zhang, Z. Liu, M. Cao, M. N. Ateş, Y. Li, L. Chen, Z. Wang and X. Wang, *Nano-Micro Lett.*, 2023, **15**, 215.
7 R. Mo, X. Tan, F. Li, R. Tao, J. Xu, D. Kong, Z. Wang, B. Xu, X. Wang and C. Wang, *Nat. Commun.*, 2020, **11**, 1374.

8 J. H. Park, H. Yoon, Y. Cho and C.-Y. Yoo, *Materials*, 2021, **14**, 4683.
9 T. G. Tran, H. D. Ngo, L. T. Pham, M. Van Tran, T.-A. Nguyen, H. T. Bui, N. P. T. Le, T. N. T. Bui, D. Q. Nguyen and T. L. Nguyen, *J. Mater. Sci.: Mater. Electron.*, 2025, **36**, 1280.
10 K. Kumar and R. Kundu, *Chem. Rec.*, 2025, e202500182.
11 D. Ma, Z. Cao and A. Hu, *Nano-Micro Lett.*, 2014, **6**, 347–358.
12 P. U. Nzereogu, A. D. Omah, F. I. Ezema, E. I. Iwuoha and A. C. Nwanya, *Appl. Surf. Sci. Adv.*, 2022, **9**, 100233.
13 X. Zhu, *J. Energy Storage*, 2022, **49**, 104148.
14 Q. Ma, J. Sha, B. Chen, E. Liu, C. Shi, L. Ma, F. He, C. He, N. Zhao and J. Kang, *J. Mater. Chem. A*, 2025, **13**, 22009–22019.
15 C. Cheng, F. Chen, Y. Cheng and G. Lai, *Ceram. Int.*, 2022, **48**, 26393–26399.
16 V. D. Phung, T. G. Tran, D. Q. Nguyen, N. H. T. Tran, K. J. Kim, D. Chun, T. L. Nguyen and J. Moon, *Ceram. Int.*, 2024, **50**, 52302–52313.
17 A. Cholewinski, P. Si, M. Uceda, M. Pope and B. Zhao, *Polymers*, 2021, **13**, 631.
18 X. Zhao, S. Niketic, C.-H. Yim, J. Zhou, J. Wang and Y. Abu-Lebdeh, *ACS Omega*, 2018, **3**, 11684–11690.
19 S. Lee, H. Koo, H. S. Kang, K.-H. Oh and K. W. Nam, *Polymers*, 2023, **15**, 4477.
20 J. He, C. Das, F. Yang and J. Maibach, *Electrochim. Acta*, 2022, **411**, 140038.
21 T. G. Tran, T. N. Nguyen, N. P. T. Le, L. T. Pham, M. V. Tran, Q. Q. Viet Thieu, T. L. Nguyen and D. Q. Nguyen, *Ceram. Int.*, 2024, **50**, 43710–43718.
22 X. Deng, X. Zhao, X. Zhang, L. Zhang and J. Zhang, *Inorg. Chem. Commun.*, 2025, 115439.
23 M. Shetty, M. Murthy, M. Shastri, M. Sindhusree, H. P. Nagaswarupa, P. D. Shivaramu and D. Rangappa, *Ceram. Int.*, 2019, **45**, 24965–24970.
24 X. Zhai, J. Gao, R. Xue, X. Xu, L. Wang, Q. Tian and Y. Liu, *J. Colloid Interface Sci.*, 2018, **518**, 242–251.
25 Y. Li, M. A. Trujillo, E. Fu, B. Patterson, L. Fei, Y. Xu, S. Deng, S. Smirnov and H. Luo, *J. Mater. Chem. A*, 2013, **1**, 12123–12127.
26 H. Wang, H. Yang and L. Lu, *RSC Adv.*, 2014, **4**, 17483–17489.
27 Z. Li, W. Zhang, Y. Tan, J. Hu, S. He, A. Stein and B. Tang, *Electrochim. Acta*, 2016, **214**, 103–109.
28 W. Fang, N. Zhang, L. Fan and K. Sun, *Electrochim. Acta*, 2017, **238**, 202–209.
29 J. Lei, Y. Liu, Y. Cheng, L. Wang, Y. Chen, C. Liang and F. Wang, *ACS Appl. Nano Mater.*, 2024, **7**, 9403–9411.
30 Y. Liang, Z. G. Tian, H. J. Liu and R. Peng, *J. Alloys Compd.*, 2010, **504**, 50–52.
31 G. Tian, Y. Chen, W. Zhou, K. Pan, Y. Dong, C. Tian and H. Fu, *J. Mater. Chem.*, 2011, **21**, 887–892.
32 J. Li, X. Liu, Z. Sun, Y. Sun and L. Pan, *J. Colloid Interface Sci.*, 2015, **452**, 109–115.
33 P. Kour, K. Hussain, P. Chand, J. N. Babu, C. S. Yadav, J. Garcia, S. K. Sharma and K. Yadav, *Mater. Adv.*, 2025, **6**, 5310–5323.
34 R. Wang, D. Li, H. Wang, C. Liu and L. Xu, *Nanomaterials*, 2019, **9**, 1341.
35 K. Čech Barabaszová, S. Holešová, L. Plesník, Z. Kolská, K. Joszko and B. Gzik-Zroska, *Polymers*, 2022, **14**, 3831.
36 M. Xie, L. Li, K. Yuan, Y. Ma and B. Liu, *J. Mater. Sci.: Mater. Electron.*, 2019, **30**, 2030–2036.
37 J. A. L. Soo, M. M. Z. Makhtar, N. F. Shoparwe, T. A. Otitoju, M. Mohamad, L. S. Tan and S. Li, *Membranes*, 2021, **11**, 676.
38 J.-T. Li, X.-S. Jia, G.-F. Yu, X. Yan, X.-X. He, M. Yu, M.-G. Gong, X. Ning and Y.-Z. Long, *Nanoscale Res. Lett.*, 2016, **11**, 426.
39 L. Wang, L. Cui, Y. Liu, J. Riedel, X. Qian and Y. Liu, *Adsorpt. Sci. Technol.*, 2018, **36**, 1734–1743.
40 S. Marasini, H. Yue, S. L. Ho, H. Cha, J. A. Park, K. Jung, A. Ghazanfari, M. Y. Ahmad, S. Liu, K. Chae, Y. Chang and G. H. Lee, *Bull. Kor. Chem. Soc.*, 2020, **41**, 829–836.
41 W. Kam, C.-W. Liew, J. Y. Lim and S. Ramesh, *Ionics*, 2014, **20**, 665–674.
42 P. Zhang, D. Wang, Q. Zhu, N. Sun, F. Fu and B. Xu, *Nano-Micro Lett.*, 2019, **11**, 81.
43 T. Zhang, E. Olsson, M. Choolaei, V. Stolojan, C. Feng, H. Wu, S. Wang and Q. Cai, *Materials*, 2020, **13**, 1132.
44 N. Lingappan, L. Kong and M. Pecht, *Renewable Sustainable Energy Rev.*, 2021, **147**, 111227.
45 T. L. Nguyen, D. Park and I. T. Kim, *J. Nanosci. Nanotechnol.*, 2019, **19**, 6636–6640.
46 M. Srivastava, A. K. M. Reddy and K. Zaghib, *Batteries*, 2024, **10**, 268.
47 T. Qin, H. Yang, Q. Li, X. Yu and H. Li, *Ind. Chem. Mater.*, 2024, **2**, 191–225.
48 P. Mandal, K. Stokes, G. Hernández, D. Brandell and J. Mindemark, *ACS Appl. Energy Mater.*, 2021, **4**, 3008–3016.
49 X. Pu, D. Zhao, C. Fu, Z. Chen, S. Cao, C. Wang and Y. Cao, *Angew. Chem., Int. Ed.*, 2021, **60**, 21310–21318.
50 P. Parikh, M. Sina, A. Banerjee, X. Wang, M. S. D'Souza, J.-M. Doux, E. A. Wu, O. Y. Trieu, Y. Gong, Q. Zhou, K. Snyder and Y. S. Meng, *Chem. Mater.*, 2019, **31**, 2535–2544.
51 H. Liu, J. Sun, P. Sun, C. Zhao, T. Ma, X. Shi, Y. Wang and Y. Wei, *Small*, 2025, **21**, 2503069.
52 L. Zhong, Y. Sun, K. Shen, F. Li, H. Liu, L. Sun and D. Xie, *Small*, 2024, **20**, 2407297.
53 X. H. Rui, N. Ding, J. Liu, C. Li and C. H. Chen, *Electrochim. Acta*, 2010, **55**, 2384–2390.
54 T. L. Nguyen, V. D. Phung, K. Ayalew, D. Chun, I. T. Kim, K. J. Kim and J. Moon, *Chem. Eng. J.*, 2021, **415**, 128813.
55 W. Qi, J. G. Shapter, Q. Wu, T. Yin, G. Gao and D. Cui, *J. Mater. Chem. A*, 2017, **5**, 19521–19540.
56 H. Sh. Majdi, Z. A. Latipov, V. Borisov, N. O. Yuryevna, M. M. Kadhim, W. Suksatan, I. H. Khlewee and E. Kianfar, *Nanoscale Res. Lett.*, 2021, **16**, 177.
57 T. G. Tran, T. L. Nguyen, D. Q. Nguyen, N. T. Tran, T. M. Dung Ngo, L. T. Pham, M. Van Tran, H. D. Ngo, H. T. Bui, T. T. Kieu Ngan and I. T. Kim, *Ceram. Int.*, 2025, DOI: 10.1016/j.ceramint.2025.05.270.
58 R. Jin, Y. Cui, Q. Wang and G. Li, *J. Colloid Interface Sci.*, 2017, **508**, 435–442.
59 S. Jin, N. Li, H. Cui and C. Wang, *Nano Energy*, 2013, **2**, 1128–1136.